Brain Stimulation 17 (2024) 561–571

Contents lists available at ScienceDirect

Brain Stimulation

journal homepage: www.journals.elsevier.com/brain-stimulation

Transcranial electric stimulation modulates firing rate at clinically relevant intensities

Forouzan Farahani [a], Niranjan Khadka [a], Lucas C. Parra [a], Marom Bikson [a], Mihály Vöröslakos [b,*]

[a] Department of Biomedical Engineering, The City College of New York, New York, NY, USA
[b] Neuroscience Institute and Department of Neurology, NYU Grossman School of Medicine, New York University, New York, NY, USA

ARTICLE INFO

Keywords:
Transcranial electric stimulation
Computational modeling
Single-unit effects

ABSTRACT

Background: Notwithstanding advances with low-intensity transcranial electrical stimulation (tES), there remain questions about the efficacy of clinically realistic electric fields on neuronal function.
Objective: To measure electric fields magnitude and their effects on neuronal firing rate of hippocampal neurons in freely moving rats, and to establish calibrated computational models of current flow.
Methods: Current flow models were calibrated on electric field measures in the motor cortex (n = 2 anesthetized rats) and hippocampus. A Neuropixels 2.0 probe with 384 channels was used in an in-vivo rat model of tES (n = 4 freely moving and 2 urethane anesthetized rats) to detect effects of weak fields on neuronal firing rate. High-density field mapping and computational models verified field intensity (1 V/m in hippocampus per 50 μA of applied skull currents).
Results: Electric fields of as low as 0.35 V/m (0.25–0.47) acutely modulated average firing rate in the hippocampus. At these intensities, firing rate effects increased monotonically with electric field intensity at a rate of 11.5 % per V/m (7.2–18.3). For the majority of excitatory neurons, firing increased for soma-depolarizing stimulation and diminished for soma-hyperpolarizing stimulation. While more diverse, the response of inhibitory neurons followed a similar pattern on average, likely as a result of excitatory drive.
Conclusion: In awake animals, electric fields modulate spiking rate above levels previously observed in vitro. Firing rate effects are likely mediated by somatic polarization of pyramidal neurons. We recommend that all future rodent experiments directly measure electric fields to insure rigor and reproducibility.

1. Introduction

The effects of transcranial electric stimulation on neural activity in the brain have been known since the 1960 [1–3]. The acute effects on neuronal firing rate are particularly well established. Namely, the electric fields generated within the brain by transcranial current stimulation can incrementally polarize cell membranes [4] and thus modulate ongoing cell firing [5,6]. The effect acts at the time scale of the neuronal membrane (~30 ms) and thus is relevant for direct current (DC) and most effective for alternating currents (AC) of 30 Hz or less [7,8]. This acute neuromodulatory effect can be predicted from the orientation and intensity of local electric fields [9,10]. These cellular mechanisms established with in vitro animal experiments, also point to network effects [11,12], which can be properly studied only in the intact brain.

However, despite numerous in-vivo animal studies in the intervening decades [12–24], there is still a lack of clarity as to whether the effects observed are clinically relevant, for one simple reason: in vivo animal experiments have not adequately characterized electric field magnitudes in the brain. In particular, a significant gap has emerged [25] between electric fields measured in vivo in the human brain, which are at or below 0.5 V/m [19,26,27] and field intensities used for in vitro animal experiments, which are mostly at or above 5 V/m [28]. Thus, it is difficult to interpret and link results from in vivo animal experiments to cellular effects observed in vitro. Nor is it clear that the in vivo animal experiments have any relevance to the behavioral effects observed in human clinical studies.

To close this gap, we measured electric fields magnitude and their effects on neuronal firing rate in vivo in rats and established calibrated computational models of current flow. To do so, we first calibrated our recording equipment on a phantom, and performed in vivo field measurements in cortex and hippocampus in a rodent tES model. Then, using

* Corresponding author.
E-mail address: mihaly.voroslakos@nyulangone.org (M. Vöröslakos).

https://doi.org/10.1016/j.brs.2024.04.007
Received 20 December 2023; Received in revised form 25 March 2024; Accepted 11 April 2024
Available online 15 April 2024

high-channel count probes (Neuropixels2.0 [29]) we analyzed firing rate of individual putative pyramidal and interneurons in response to short DC stimulation. This is best done in the hippocampus because there is a well-defined orientation of pyramidal neurons relative to the applied electric field [30], and we can distinguish between putative pyramidal and interneurons using extracellular recordings [31] and optogenetic stimulation [32–35]. Our hypothesis is that firing rate is modulated by acute somatic membrane polarization [6,7]. Therefore, we will measure firing rate effects on a short time scale of 3s, which allows for repeated trials to identify small effects. To distinguish from the usual 20 min constant current stimulation protocol of tDCS, we refer to stimulation here as tES.

2. Methods

2.1. Characterization of recording and stimulation system using agar phantom

Brain phantom was constructed using a 26.7 mm diameter spherical container (30 ml syringe). To provide T1 and T2 relaxation comparable to gray matter, we followed the recipe by Schneiders et al. [36]. A 10 mM Nickel Chloride mixture was prepared: 2.377 g [Ni(Cl2)·6H2O] per 1 L H2O * 2.377 g of Nickel Chloride in 1 L of distilled water. The agar mixture was prepared as: 3600 ml H2O, 400 ml 10 mM Ni(Cl2), 120 g Agar, 20 g NaCl (0.5 %) and 1 g of Sodium Azide. The mixture was heated until boiling until the agar was completely dissolved. The boiling liquid was poured into the phantom using a funnel. All air bubbles were removed by creating a vacuum in the syringe. The phantom was let cool down and a 30-mm cylinder was cut for in vitro calibration of recording and stimulation devices (Suppl. Fig. 1A).

High-pass filtering is inherent in the design of extracellular electrophysiology amplifiers, with bandwidths ranging from 0.1 to 10 kHz [37]. To confirm the accuracy of our recording system (RHD USB Interface Board, Intan Technologies) and determine if any signal distortion is introduced, we applied stimulation at different frequencies (1, 10, 100 and 1000 Hz) and at different intensities (100, 150 and 200 μA, Suppl. Fig. 1A) to an agar phantom [36,38]. The phantom was a homogeneous cylinder of 20 mm in height and 26.7 mm in diameter that was filled with agar with conductivity $\sigma = 0.9$ S/m (Suppl. Fig. 1B). Stimulation was delivered using platinum electrodes (2.2 by 1.6 mm) positioned at a separation of 17.81 mm using an isolated stimulus generator (STG 4002, Multichannel Systems). For the measurement of the voltage values generated during stimulation within the phantom, we used two custom-built tungsten electrodes (two recording channels each electrode, 56.3 ± 19.8 kOhm impedance at 1 kHz, mean ± SD, Suppl. Figs. 1B and C and Suppl. Fig. 2 and Suppl. Video 1). The tungsten electrodes were attached to a microdrive [39] and positioned 3.4 mm apart using a stereotactic frame (Model 962, David Kopf Instruments, Suppl. Figs. 1B and D). The magnitude of the electric field increased linearly with stimulation intensities as expected (100, 150 and 200 μA, Suppl. Fig. 1E). However, the slope of the electric field decreased during 1 Hz stimulation (Suppl. Fig. 1E) reflecting signal attenuation caused by the built-in 0.7 Hz high-pass filter in the recording system.

2.2. Preparing tungsten recording device

A 26-gauge needle was cut to 3 mm. 50-μm tungsten wires (Tungsten 99.95 %, 100211, insulated with Heavy Polyimide, HML – Green, California Fine Wire, CA) were cut to 30 mm and the insulation (green coating) was removed from one end using a razor blade. Two tungsten wires were inserted into the stainless-steel tube (2-channel shank). Wires were positioned 5 mm from the end of the tube. Wires were separated (ch-1 and ch-2) 1 mm apart from each other (Suppl. Fig. 3). Ultra-liquid superglue (Loctite 1647358, Henkel, Germany) was applied on both ends of the tube and between wires. Two, 2-channel, single shank devices were attached to a mechanical shuttle (microdrive) or a 2 by 4 mm printed circuit board) making a 4-channel, 2-shank device. For the motor cortex recording wires were bent 90°. Tungsten wires and a ground wire were soldered inside a header pin (575–8514305010, Mouser, TX). The header pin connector to Omnetics adapter was soldered to connect tungsten wires to preamplifier headstage (#C3324, Intan Technologies Inc., CA). Impedance of the wires were measured by RHD USB interface board from Intan (Intan Technologies LLC, CA, USA). The device was lowered into 0.9 % saline and connected to the recording preamplifier ground (RHD 32-channel recording headstages). Impedance measurement was performed at 1 kHz frequency.

2.3. Experiments on rats

All experiments were approved by the Institutional Animal Care and Use Committee at New York University Medical Center and CUNY IACUC. Rats (adult male n = 7 and female n = 1, 300–400 g) were kept in a vivarium on a 12-h light/dark cycle and were housed two per cage before surgery. Rats were implanted with custom-made recording and stimulating electrodes under urethane anesthesia (1.3–1.5 g/kg, intraperitoneal injection). Atropine (0.05 mg kg–1, s.c.) was administered after anesthesia induction to reduce saliva production. The body temperature was monitored and kept constant at 36–37 °C with a DC temperature controller (TCAT-LV; Physitemp, Clifton, NJ, USA). Stages of anesthesia were maintained by confirming the lack of a nociceptive reflex.

2.4. Stimulation and recording of electric fields in motor cortex of anesthetized rats

The chest wall and the head were shaved. We made an incision on the head and on the chest wall. A 10 by 10 mm platinum mesh electrode (Goodfellow, PT00-MS-000110) was sutured to the pectoral muscle and an insulated cable was tunneled to the top of the head of the animal. The skull was cleaned by hydrogen peroxide (2 %) and a stimulation pocket was attached to the skull using dental cement (1.5 mm anterior to bregma and 3 mm lateral to midline). The pocket was filled with conductive gel (Signagel Electrode Gel) and a 3 by 3 mm platinum stimulation electrode was inserted inside. The pocket is open at one side to expose the skull to the electrode and gel, but isolate it from surrounding tissues. A craniotomy was performed on the temporal bone (1.44 mm anterior from bregma and 3 mm deep from the top of the skull) and the dura was removed. The tungsten device was inserted to the target depth (2.4 mm from the surface of the brain). The collected data was digitized at 20 kS/s using an RHD2000 recording system (Intan Technologies, Los Angeles, CA). Stimulation was delivered by Caputron LCI 1107 High Precision. Varying frequencies (10, 100 and 1000 Hz) at varying intensities (10, 20 and 40 μA) were delivered through the stimulating electrodes. Electric field was measured by fitting a sinusoid to the recorded voltage differences between the 4 contacts, averaging amplitudes of the two parallel measures, and dividing by the electrode distance (1 mm). This results in a 2D field vector, with magnitude given by the norm of this vector.

2.5. Stimulation and recording of in hippocampus of anesthetized and freely moving rats

The skin of the head was shaved. After a midline incision the surface of the skull was cleaned by hydrogen peroxide (2 %). A custom stimulation pocket was attached to the skull using dental cement (4.8 mm posterior from bregma). The pocket was filled with conductive gel (SuperVisc, EasyCap GmBH, Germany) and a 2 by 2 mm platinum stimulation electrode (#349356-600 MG, Sigma-Aldrich, Inc., St. Louis, MO) was inserted inside. A stainless-steel ground screw was placed above the cerebellum (#90910A380, McMaster-Carr, Elmhurst, IL). A craniotomy was performed (4.8 mm posterior from Bregma and 5 mm lateral to midline) and the dura was removed. The silicon probe was

attached to a microdrive [39] (128-5, Diagnostic Biochips Inc., Glen Burnie, MD or Neuropixels 2.0) and it was inserted to the target depth (4 and 6 mm from the surface of the brain). We constantly monitored the electrophysiological signal during insertion. The collected data (128-5 probe) was digitized at 20 kS/s using an RHD2000 recording system (Intan Technologies, Los Angeles, CA). Neuropixels2.0 data was digitized at 30 kS/s and a custom PXIe (Peripheral Component Interconnect (PCI) eXtension for Instrumentation; a standardized modular electronic instrumentation platform) data acquisition card was connected to a computer via a PXI chassis (NI 1071, National Instruments, Austin, TX), and OpenEphys software was used to write the data to disk [40,41]. Baseline session (1 h before tES) and electrical stimulation session were recorded in the homecage of rats during the sleep cycle of the animals. Stimulation was delivered by an STG4002–16 mA (Multi Channel Systems, Reutlingen) using different intensities and polarities (Suppl. Table 1). Rats did not show any behavioral response to stimulation. To measure the electric fields in the hippocampus, varying frequencies (10, 100 and 1000 Hz) at varying intensities (10, 20 and 30 μA) were delivered through the stimulating electrodes at the end of the recording session. tES induced voltage changes were measured shank-by-shank (4*384 = 1536 recording sites in total). Electric field was measured by fitting a sinusoid to the recorded voltage at each recording site. We first calculated the average peak-to-peak voltage on each site (n = 500 cycles), and then calculated the first spatial derivative of these voltage values across shanks. An average hippocampal electric field was calculated after localizing the cellular layer of the hippocampus using electrophysiological markers (Fig. 2, n = ± 32 channels were averaged around the center of the pyramidal layer). The same preparation was used to record local field potentials and single unit activity.

2.6. Local field potential analysis

To detect sharp wave ripples a single electrode in the middle of the pyramidal layer was selected. The wide-band LFP signal was band-pass filtered (difference-of-Gaussians; zero-lag, linear phase FIR), and instantaneous power was computed by clipping at 5 SD, rectified and low-pass filtered. The low-pass filter cut-off was at 55 Hz, and the band-pass filter was from 80 to 200 Hz. Subsequently, the power of the non-clipped signal was computed, and all events exceeding 5 SD from the mean were detected. Events were then expanded until the (non-clipped) power fell below 2 SD; short events (<15 ms) were discarded. The pyramidal layer of the CA1 region was identified physiologically by increased unit activity and characteristic LFP patterns. Here we are benefiting from the laminar organization of the hippocampus with a well defined orientation relative to the applied electric fields.

2.7. Single unit analysis

A concatenated signal file was prepared by merging all recordings from a single animal from a single day. To improve the efficacy of spike sorting, stimulation induced onset and offset artefacts were removed before automatic spike sorting (10 ms before and 100 ms after the detected artefacts, linear interpolation between timestamps). Putative single units were first sorted using Kilosort [30] and then manually curated using Phy (https://phy-contrib.readthedocs.io/). After extracting timestamps of each putative single unit activity, peristimulus time histograms and firing rate gains were analyzed using a custom MATLAB (Mathworks, Natick, MA) script. Changes in firing rate of single units (ΔF) were calculated by the following equation:

$$\Delta F = 100 * \frac{\underline{S} - \underline{N}}{max\ (S, N)},$$

Where $\underline{S}$ and $\underline{N}$, are the mean firing rates for the stimulation (S) and no stimulation (N) epochs. Cells were classified into three putative cell types: narrow interneurons, wide interneurons, and pyramidal cells based on waveform metric [42].

2.8. Cell type classification

In the processing pipeline, cells were classified into two putative cell types: interneurons, and pyramidal cells. Interneurons were selected by two separate criteria. We labeled single units as interneurons if their waveform trough-to-peak latency was <0.425 ms, or if the waveform trough-to-peak latency was >0.425 ms and the rise time of the auto-correlation histogram was >6 ms. The remaining cells were assigned as pyramidal cells. Autocorrelation histograms were fitted with a triple exponential equation to supplement the classical, waveform feature based single unit classification (https://cellexplorer.org/pipeline/cell-type-classification/) [42]. Bursts were defined as groups of spikes with interspike intervals <9 ms [31,32,43,44]. The authors had isolated 762 putative single units from seven animals in nine sessions (n = 453 putative pyramidal cells, n = 193 putative interneurons). Similar categorization of cell type from cortical recordings is more difficult given a sparsity of ground truth data, which is one of the reasons why we selected to study firing rate effects in the hippocampus.

2.9. Detection of monosynaptic cell pairs

Cross-correlation (CCG) analysis has been applied to detect putative monosynaptic connections [33,45]. CCG was calculated as the time resolved distribution of spike transmission probability between a reference spike train and a temporally shifting target spike train. A window interval of [−5, +5] ms with a 1-ms bin size was used for detecting sharp peaks or troughs, as identifiers of putative monosynaptic connections. Significantly correlated cell pairs were identified using a previously ground-truth validated convolution method [33]. The reference cell of a pair was considered to have an excitatory monosynaptic connection with the referred neuron, if any of its CCG bins within a window of 0.5–3 ms reached above confidence intervals.

2.10. Modeling of current-induced fields

Magnetic resonance imaging (MRI) scan of a template rat head was segmented into scalp, skull, cerebrospinal fluid (csf), gray matter, white matter, cerebellum, hippocampus, thalamus, and air to develop a high resolution (0.1 mm) volume conductor model in Simpleware (Synopsys Inc., CA, USA) using both automatic and manual filters. Computer aided model (CAD) geometry of the electrodes was modeled in SolidWorks (Dassault Systemes Corp., MA, USA) and positioned based on coordinates value from the experiment. Specifically, we modeled two montages to predict the electric field in the motor cortex (montage 1) and hippocampus (montage 2). In montage 1, Platinum plate electrode ($3 \times 3 \times 0.1$ mm^3) was positioned above the primary motor cortex (2 mm lateral and 1.5 mm anterior from bregma) over the exposed skull by smearing a thin layer of conductive electrode gel, whereas the return electrode (Platinum mesh) was placed inside the chest wall ($10 \times 10 \times 1$ mm^3). In montage 2, a Platinum plate electrode ($2 \times 2 \times 0.1$ mm^3) was immersed into a conductive electrode gel and secured over the temporal bone by a plastic electrode holder on each hemisphere of the rodent head.

An adaptive tetrahedral mesh of rat model resulting from multiple mesh refinements was generated using a voxel-based meshing algorithm and contained >8 M tetrahedral elements and was solved for >10 million degrees of freedom. Volumetric meshes were later imported into COMSOL Multiphysics 5.5 (COMSOL Inc., MA, USA) to solve the model computationally using a steady-state assumption (Laplace equation, $\nabla(\sigma\nabla V) = 0$, where V = potential and σ = conductivity). Compartment-specific assigned electrical conductivities were given as, scalp: 0.465 S/m; skull: 0.01 S/m; csf: 1.65 S/m; air: 1 × 10-15; gray matter: 0.276 S/m; cerebellum: 0.276 S/m; hippocampus: 0.126 S/m; white matter: 0.126 S/m; thalamus: 0.276 S/m, electrode: 5.99 × 107 S/m, conductive gel:

4.5 S/m, and plastic electrode holder 1 × 10-15 S/m. All values were based on prior literature [46]. The boundary conditions were applied as current (Montage 1: 40 μA and Montage 2: 100 μA) at the exposed surface of the skull electrode while the contralateral electrode was grounded. All remaining outer boundaries of both models were electrically insulated. Electric field at the primary motor cortex and hippocampus, mimicking experimental recording sites, was predicted and peak value was reported. Specifically, an electric field magnitude slice at the center of the skull electrode was plotted in the coronal and sagittal plane in montage 1 (Fig. 1E), whereas in montage 2, the electric field magnitude slice plot was taken coronally at the center of the skull attached tES electrodes (Fig. 2G). Electric field magnitude as a function of distance from the cortical surface moving in radial direction was plotted in the coronal plane for montage 1 (Fig. 1F) and in horizontal direction in montage 2 (Fig. 2H).

2.11. Statistical analysis

Based on our previous studies we expected to successfully record firing rate in ~100 neurons per animal with 100 trials per condition giving us adequate power to detect relatively small effects on firing rate within cell and animal. The number of animals was selected primarily to capture variation in field magnitude across animals due to the exact location of recording electrodes. No rats were excluded from the analysis. Each animal served as its own control, no randomization or blinding was employed. Statistical analyses were performed with MATLAB functions or custom-made scripts. To measure the effect of electrical stimulation on spiking, peristimulus time histograms (PSTHs) were built around stimulus onset (spike trains were binned into 10-ms bins). Baseline and tES-induced firing rate were calculated for each single unit. Baseline was defined as tES-free epochs (3 or 4 s) between trials and stimulation period as the electrical stimulation was on (3 or 4 s). Firing rate change was measured in percent by dividing spike count with the mean count per neuron (taking maximum of stimulation and baseline mean counts) times 100. Where we analyze effects (firing rate change or field magnitude) as a function of stimulation intensity we report Pearson's correlation coefficient R with corresponding p-values. To measure the efficacy of stimulation at the lowest intensity tested (±25 μA in 3 freely moving rats) we combine firing rate changes across all trials and neurons and compute slope as % change in firing rate per

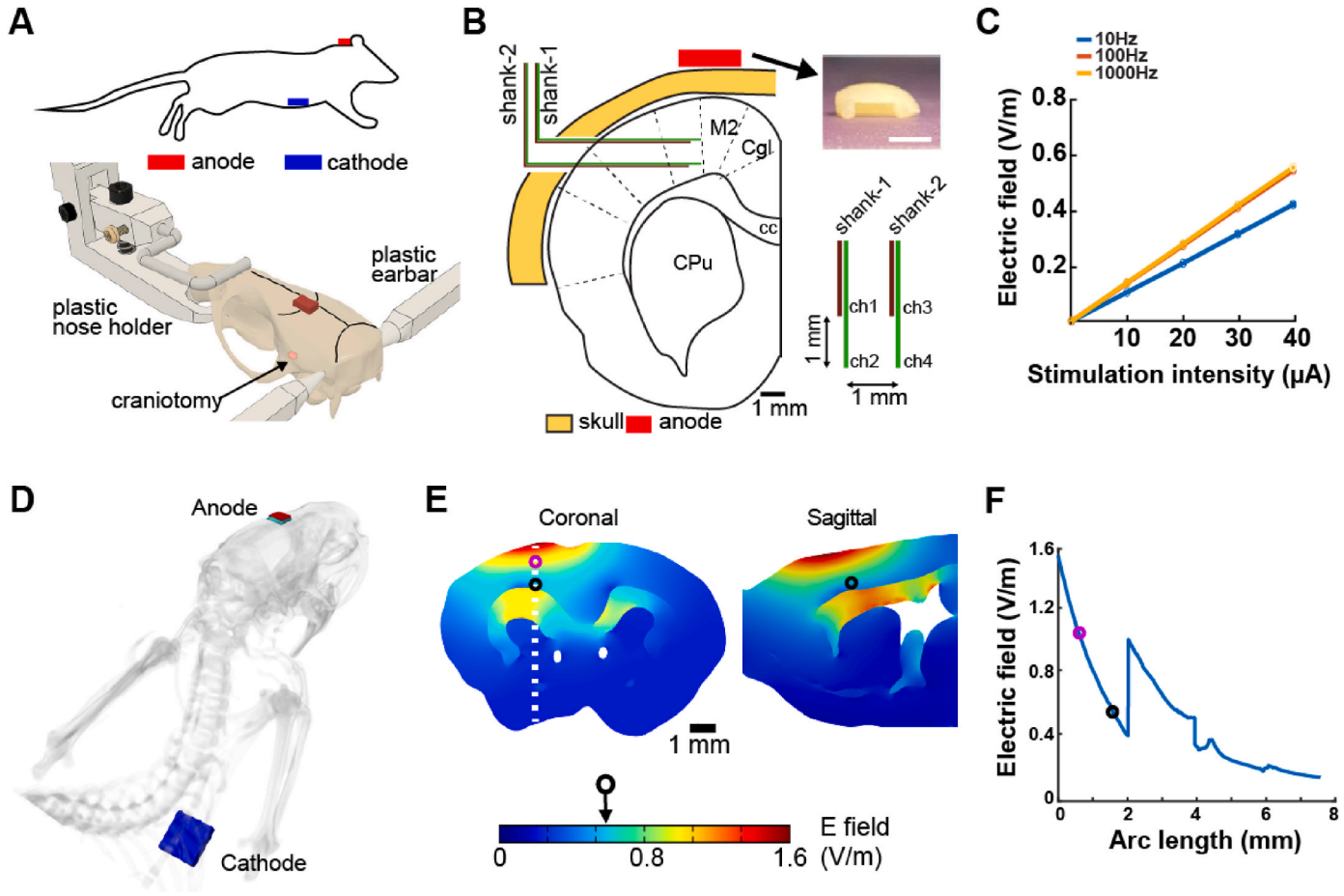

Fig. 1. Measurement and modeling of tES-induced electric field in motor cortex. (A) Electric field measurement in the motor cortex of rats. Top: An electrode is affixed to the skull above the primary motor cortex (3 by 3 mm platinum plate, anode), and a return electrode is implanted inside the chest wall (10 by 10 mm platinum mesh, cathode). Bottom: 3D-printed nose holders and ear bars are used to isolate the animal from the metallic components of the stereotactic frame during measurements. The rat skull is shown inside the nose holder with skull electrode (red rectangle) and craniotomy in the parietal bone. **(B)** Schematic of the position of recording electrodes in the motor cortex. Note that electrodes were inserted from the lateral side of the skull through the temporal craniotomy. Top, right: Customized holder for the stimulation electrode (scale bar is 3 mm). Bottom, right: schematic of the custom-built, 2-shank, 4-channel tungsten recording matrix. Each shank had 2 recording channels (both ch1 and ch2 and shank-1 and shank-2 are separated by 1 mm). **(C)** Increasing stimulation intensity induces an increasing electric field in the motor cortex. The reduced slope of the 10 Hz condition could be induced by the built-in 0.7 Hz high-pass filter of the preamplifier. **(D)** Anatomically accurate FEM model including skull electrode (red) and gel (green) and chest electrode (blue). **(E)** Distribution of field magnitude estimated with the current flow model in the coronal and sagittal plane at 40 μA current. **(F)** Field amplitude as a function of distance from the cortical surface moving in radial direction (Arc length). The discontinuity is due to a discontinuity in conductivity (white matter of corpus colosseum has lower conductivity than gray matter, 0.126 S/m vs 0.276 S/m). (For interpretation of the references to colour in this figure legend, the reader is referred to the Web version of this article.)

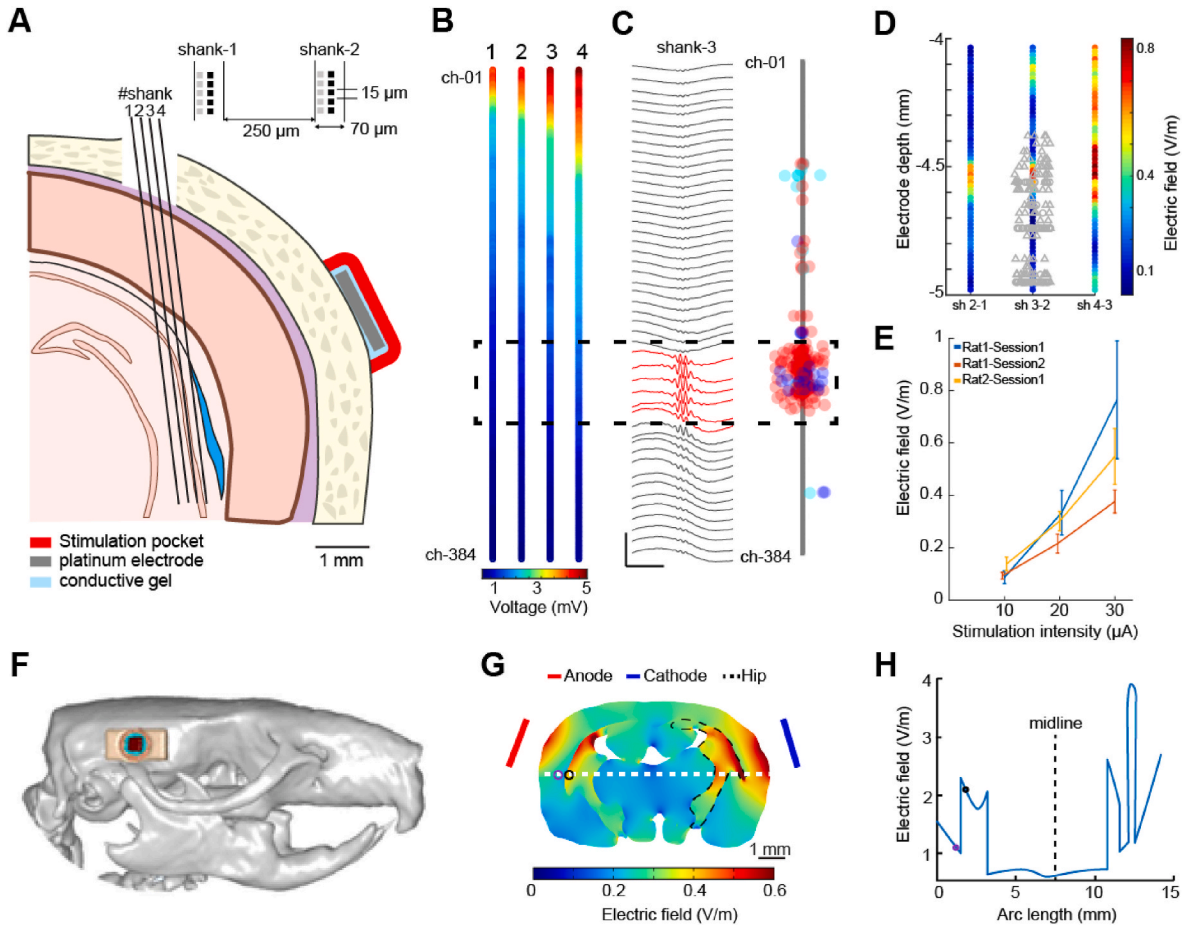

Fig. 2. Measurement and modeling of tES-induced electric field in hippocampus. (A) Electric field measurement in the hippocampus of freely moving rats. Anode and cathode are placed on the temporal bone (2 by 2 mm platinum plate). Multi-shank, multi-site silicon probe is used to measure the electric field (probe is inserted at 10°), details of the shanks are shown on the right. (B) tES-induced (30 μA, 100 Hz) peak-to-peak voltage changes measured in 4 shanks. Colors indicate the peak-to-peak average measured on each channel (n = 500 repetitions, n = 384 channels/shank, recorded sequentially from n = 4 shanks). Note the increasing voltage values closer to the stimulation electrode (shank-4). **(C)** Localizing cellular layer of hippocampus using electrophysiological markers. Left: ripple triggered average LFP traces recorded on shank-3 linear configuration (n = 48 channels, every 8th channel is shown). Red channels show the location of the maximum ripple amplitude. Right: schematic of shank-3 is shown with the putative location of recorded neuron somata (n = 181 putative pyramidal cells, 81 narrow interneurons and 2 wide interneurons, red, blue, and cyan circles, respectively). Single units were clustered in the cellular layers of the hippocampus (ch-01 represents brain surface). **(D)** tES-induced electric fields recorded in the cellular layer of the hippocampus (black dashed rectangle, n = 64 channels per shank). The location of recorded neuron somas is overlaid in gray on shank 3-2. **(E)** Increasing stimulation intensity (10, 20 and 30 μA) induces increasing intracerebral electric field (0.1, 0.28 and 0.56 V/m, R = 0.75, $p < 0.001$). **(F)** Electrode montage in the rat model. **(G)** Modeling results of tES-induced electric fields in the coronal plane (4.8 mm posterior from bregma) at 100 μA. **(H)** Electric field intensity along the white dotted line in panel G. The discontinuity in electric field is due to discontinuity in conductance between white and gray matter (see Suppl. Fig. 4). (For interpretation of the references to colour in this figure legend, the reader is referred to the Web version of this article.)

V/m (assuming 15 V/m ~ 1 mA) averaged over all neurons and trials. To obtain a null distribution for this slope, we randomize the label of stimulation intensity (−25 μA, 0 μA, 25 μA) with replacement within each trial. We repeat this bootstrapping procedure 10,000 times. Where we compare firing rates between two conditions we use a Wilcoxon rank sum test. On box plots, the central mark indicates the median, bottom and top edges of the box indicate the 25th and 75th percentiles, respectively, and whiskers extend to the most extreme data points not considered outliers. Outliers are not displayed in some plots but were included in statistical analysis. Due to experimental design constraints, the experimenter was not blind to the manipulation performed during the experiment (transcranial electrical stimulation manipulation).

3. Results

3.1. Measurement and modeling of tES-induced electric fields in motor cortex of rats

To characterize the effects of tES it is necessary to properly calibrate electric field measurements, which is the main determining factor for acute effects on neuronal function [47]. After characterizing our stimulation and recording system using agar phantom (Suppl. Fig. 1), we measured field intensity intracranially and built an anatomically detailed computational model of our electrode montage. In our experimental setup we applied sinusoidal alternating current (10, 100 and 1000 Hz at 10, 20, 30 and 40 μA intensities) in two anesthetized rats. We used sinusoidal signals because the quasi-static approximation of Maxwell's equations is valid for these frequencies in the brain [48] and extracellular amplifiers cannot measure DC potentials due to the built-in high-pass filters (bandwidths ranging from 0.1 to 10 kHz). We used low amplitude sinusoidal signals to avoid amplifier saturation during electric field measurements. To electrically isolate the animal from the metallic stereotactic frame, we 3D-printed a non-conducting nose holder and ear bars (Fig. 1A and Suppl. Fig. 2, Clear V4 resin, Formlabs) and placed the animal on a non-conducting surface. A platinum electrode was affixed to the skull over the forelimb motor cortex (1.5 mm anterior to bregma and 3 mm lateral from midline) within a chamber loaded with conductive gel. The pocket to hold gel and tES electrode was made of

dental cement (Figs. 1B and 3 by 3 mm, GC Unifast). The return electrode was a platinum mesh (10 by 10 mm) implanted in the chest wall [23] (Fig. 1A). This electrode montage provided electro-chemical stability and free range of movements in behaving rats. To measure the electric field generated by transcranial stimulation, we used a multi-channel, custom-built recording electrode matrix (n = 4 channels in total, 2 channels per shank, 1 mm distance between shanks and channels, Fig. 1B and Suppl. Fig. 3). After a craniotomy through the parietal bone, we inserted the electrode matrix into the motor cortex from the lateral side and sealed it with non-conductive silicon (Suppl. Fig. 2b, Kwik Cast silicone, Kwik-Cast). We found that electric field magnitude increased linearly with stimulation current, with similar slope at the three stimulation frequencies (Fig. 1C, slope: 15.0 V/m/mA). In a second animal we measured fields of twice this magnitude (not shown, slope 30.0 V/m).

We developed a high-resolution (0.1 mm^3) MRI-driven healthy rat computational model with eight tissue masks (see "Methods" for details) and predicted electric field magnitudes at the experimental recording sites. At the motor cortex location corresponding to the in vivo field recordings (Fig. 1E, black circle) the model estimates an electric field of 0.602 V/m (Fig. 1E). This corresponds to 15.05 V/m per mA and is within the range measured in-vivo. Although it should be noted that there is a strong gradient as one moves radially (Fig. 1F) - moving just 1 mm closer to the stimulating electrode the electric field per applied current doubles to 30 V/m per mA - and the recording matrix has 1 mm side length, which may explain the variation across animals.

3.2. *Measurement and modeling of tES-induced electric fields in hippocampus of rats*

The field measurements and model established that 40 μA stimulation can induce 0.6–1.2 V/m fields in motor areas. The exact field magnitude strongly depends on the recording location and thus, it has to be measured in the precise region of interest. We were interested in neural responses in the hippocampus, and so we decided to measure fields again with the same electrodes we will use for recording neural activity. We implanted Neuropixels (NP) 2.0 probes [29] in the intermediate CA2 region of freely moving rats (Fig. 2A, n = 2 rats, 4.8 mm posterior to bregma and 4.6 mm lateral to midline, angled at 10°). We applied electrical current through two skull electrodes (2 by 2 mm platinum plates), but this time affixed to the temporal bone bilaterally (Fig. 2A). We took advantage of the 5120 contacts available on the NP

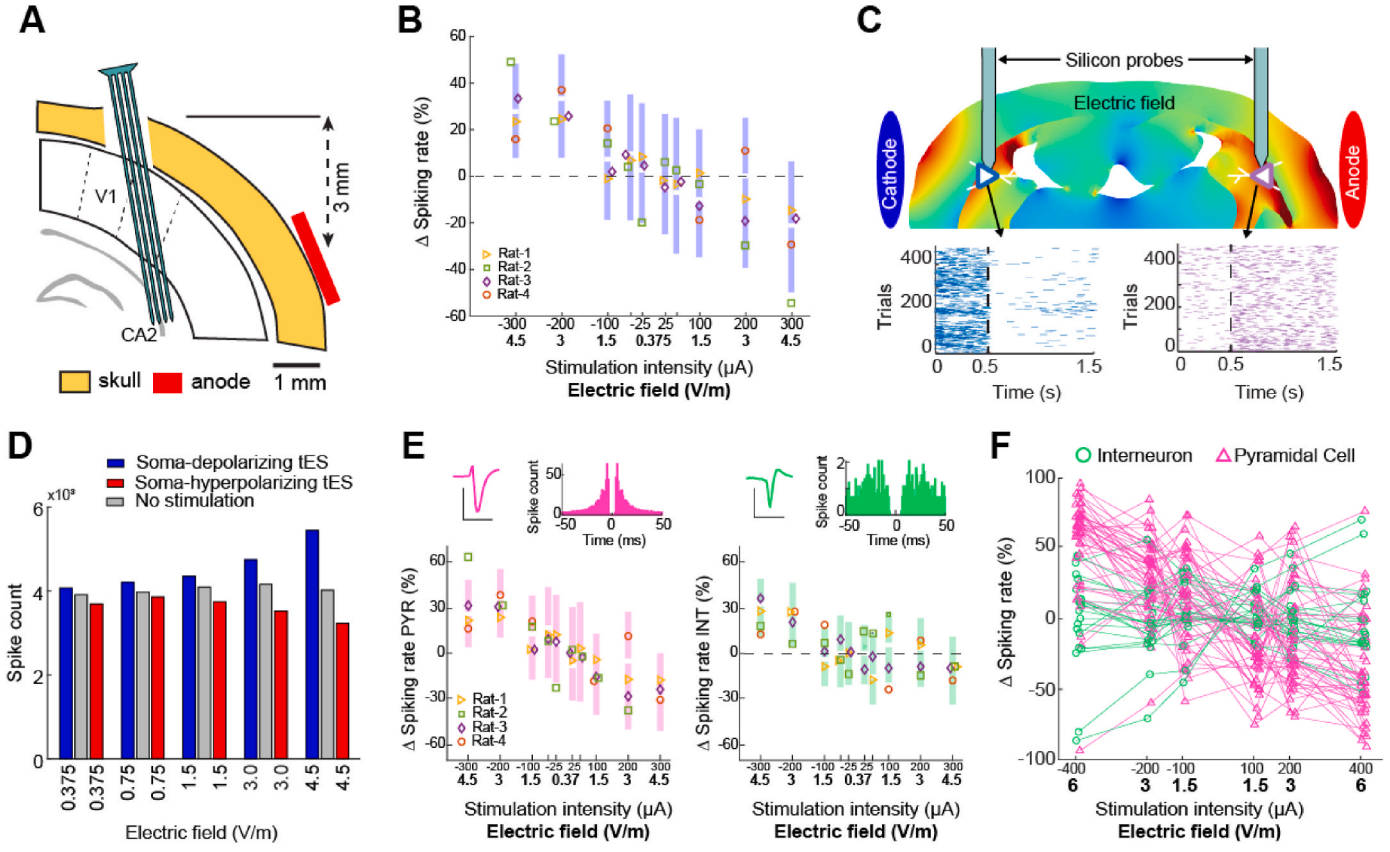

Fig. 3. Electric field dependent change of firing rate of hippocampal neurons. (A) Schematic of experimental setup. Multi-shank, multi-site silicon probe is used to measure neuronal activity in the intermediate CA2. **(B)** tES induced a polarity and intensity dependent modulation of neuronal firing in the hippocampus (R = −0.33, P < 0.001, n = 510 neurons in 4 rats). For each stimulus intensity, the generated electric field strengths are shown at the bottom of the plot in bold. **(C)** Response of two putative pyramidal cells recorded from both hippocampi simultaneously using two 32-channel silicon probes. White triangles with blue and purple outline show the location of the cells' somata overlaid on the electric field model. The neuron closer to the cathode (blue neuron) was excited by the stimulation as shown by the peristimulus time histogram. The neuron closer to the anode showed an opposite response (purple neuron). **(D)** Number of spikes during soma-depolarizing (blue), hyperpolarizing (red) tES and baseline (gray) periods. Each bar represents the total number of emitted spikes (n = 394 neurons in 3 rats). Note, the number of evoked spikes increase with intensity and reverse with polarity. **(E)** Recorded neurons are classified into putative excitatory (top, left) and putative inhibitory neurons (top, right) based on their waveform and autocorrelation histogram. The scale bar is 0.1 mV and 1 ms. Bottom: tES influenced the spiking rate of both putative pyramidal cells (bottom, left, R = −0.34, p < 0.001, n = 359 neurons in 4 rats) and putative interneurons (bottom, right, R = −0.3, p < 0.001, n = 151 neurons in 4 rats). **(F)** Some neurons were modulated in the opposite direction as the average response of the hippocampus. Note the three cells that were inhibited by soma-depolarizing and excited by soma-hyperpolarizing tES (example session from one rat). (For interpretation of the references to colour in this figure legend, the reader is referred to the Web version of this article.)

2.0 probe, to select 384 channels for recording from each shank. We chose a single shank, linear configuration spanning 5760 μm (15 μm separation per channel) to record electric potential during sinusoidal tES (100 Hz, n = 500 cycles, at 10, 20, and 30 μA intensity) sequentially from each of the 4 implanted shanks. (Fig. 2B). As expected, we recorded higher voltages on the most lateral shank (Fig. 2B, shank-4 was closest to the stimulation electrode, each shank is separated by 250 μm). Additionally, we recorded higher voltage values following the curvature of the brain surface which likely reflects shunting caused by cerebrospinal fluid in the meningeal space [27,49,50]. To measure the electric fields in the hippocampus, we first localized the cellular layer of CA2 using electrophysiological markers (Fig. 2C). The pyramidal layer of the hippocampus can be identified by the presence of sharp wave ripple oscillations and increased single unit activity [51]. The extracellular sharp wave (SPW) is produced by synchronous transmembrane currents in the apical dendrites of CA1 pyramidal cells, which is triggered by the synchronous CA3 inputs targeting the str. radiatum [52]. The CA3 volley also excites CA1 interneurons and their interaction induces the ripple oscillation (80–200 Hz) detected in the local field potential [53]. After detecting sharp wave ripples in the local field potential (LFP) signal, we calculated the ripple triggered average signal across 48 channels (Fig. 2C, left; 12-channel steps corresponding to 180 μm inter-site distance) and we identified the channel with maximum ripple power (Fig. 2C, left; highlighted channels in red). We determined the position of individual neuronal somata using spike sorting and spike-amplitude trilateration (Fig. 2C, right [42,54]). To calculate the hippocampal electric field, we used ±32 channels around the center of these soma locations (Fig. 2D). Similar to the motor cortex, we found that increasing stimulation intensity (10, 20 and 30 μA) induced increasing intracerebral electric fields (Fig. 2E, 0.1 ± 0.01, 0.28 ± 0.03 and 0.56 ± 0.11 V/m, mean ± SEM, n = 3 sessions from 2 rats, R = 0.76, $p < 0.001$). This corresponds to 10, 14 and 18.7 V/m per mA and thus somewhat less than the cortical measures, as expected. We will assume 15 V/m per mA in the remainder. To simulate our experimental setup, we placed electrodes over the parietal bone (Fig. 2F). We applied 100 μA current through one skull electrode while grounding the other skull electrode. The model predicted an electric field of 2.1 V/m in white matter and 1.2 V/m in gray matter in the hippocampus (Fig. 2G and H). This corresponds to 12–21 V/m per mA of applied current and is consistent with what we observed in the experimental recording above. As expected, the magnitude of the electric field dropped with distance from the cortex but increased at the boundary of white-gray matter transition (Fig. 2G and H).

3.3. *Intensity and polarity dependent effects of single unit activity induced by tES*

Single-unit action potentials are the most direct measurement of neural activity. We quantified how different tES intensities (25–400 μA) can affect the spiking activity of neurons in the hippocampus. These currents generate fields in the range of 0.375 V/m to 6 V/m assuming the observed 15 V/m per mA applied (Fig. 2E). We performed these measurements using the same rats where we measured electric fields and using the same recording and stimulation electrodes. tES was applied for 3 or 4 s and repeated hundreds of times with 3- or 4-s intervals of no stimulation (Suppl. Fig. 6A and Suppl. Table 1). Single-unit activity was recorded from the CA2 region (Fig. 3A, Suppl. Fig. 5) in 4 rats freely moving in their home cage, and two anesthetized rats (Suppl. Table 1) [29,40]. Depending on the polarity of the stimulation, putative single units either increased or decreased their spiking activity (Fig. 3B; slope: 3.75 % per V/m, R = −0.33, $P < 0.001$, n = 510 neurons). Mean percent change in firing rate (FR) of neurons is summarized in Supplementary Tables 2–4 (n = 510 neurons in 4 rats and n = 394 neurons in 3 rats). We have tested higher intensities in a urethane anesthetized rat and found that the effects did not saturate. Specifically, negative current stimulation (radially outward) increased the spiking rate by 37.22 ± 5.13 % (−400 μA), while positive stimulation (radially inward) decreased the activity of neurons by −25.4 ± 4.51 % (400 μA, n = 68 neurons, Suppl. Fig. 7). When we looked at the pattern of the tES induced firing rate in freely moving rats, we found that the highest intensities (±300 μA) were followed by either a rebound excitation or inhibition that is likely a network effect (Suppl. Figs. 6D and E). Comparing the effects of tES on spiking in the awake rats vs. the anesthetized rat, we found that urethane anesthesia reduced both the spiking rate of excitatory cells (0.88 ± 0.03 Hz, n = 394 neurons vs 0.42 ± 0.08 Hz, n = 47 neurons, mean ± SEM, awake vs. anesthesia, respectively, Suppl. Fig. 7C) and the dose-response curves of putative pyramidal cells (linear fit slope is ΔFR = −4.6 % per V/m, and ΔFR = −4.15 % per V/m during awake and anesthetized conditions, respectively, Suppl. Fig. 7C). To confirm the opposing effect on spiking activity of hippocampal cells underneath the anode and cathode, we recorded from both hippocampi simultaneously using two, 32-channel silicon probes in an anesthetized rat [19]. To be clear, electrode polarity (anode vs cathode) changes throughout the experiment. Our modeling results anticipated that the electric field's magnitude would be comparable in both hemispheres, but with opposing orientation relative to the orientation of pyramidal neurons. Neurons under the cathode were excited (Fig. 3C, blue neuron, putative pyramidal cell with a mean firing rate of 1.14 Hz), whereas those under the anode were inhibited during tES (Fig. 3C, purple neuron, putative pyramidal cell with a mean firing of 0.67 Hz, n = 400 trials, 500 ms stimulation followed by 1 s stimulation free epochs). This is the expected direction of effects given that hippocampal pyramidal neurons have the opposite orientation to cortical-surface neurons and therefore radially outward currents under the cathode are soma-depolarizing for hippocampal neurons, whereas radially inward currents under the anode are soma-hyperpolarizing [4,55].

To quantify the strength of the effect, in particular at lowest intensities tested (±25 μA) we analyzed the spike counts combining data across all neurons (Fig. 3D). The sensitivity measured as % firing rate change over applied electric field was 11.3 % per V/m (7.2, 16.0, 18.3 for the 3 animals that were measured at ±25 μA, $p < 0.0001$ bootstrap shuffling −25, 0, +25 stimulation labels, n = 62712, 43392, 11037 trials). An example where firing rate modulation at low stimulation intensities is evident at the single neuron level is shown in the supplement (Suppl. Figs. 6B and C). In the freely behaving animals, single units were classified into putative pyramidal cell and interneuron types based on waveform and spike train characteristics (Fig. 3E, top; see Methods and Suppl. Fig. 8). Stimulation exerted clear and predictable effects on the spiking rate of putative pyramidal cells (Fig. 3E, left; R = −0.34, $p < 0.001$, n = 359 putative pyramidal cells) and putative interneurons (Fig. 3E, right; R = −0.3, $p < 0.001$, n = 151 putative interneurons). Further analysis of cell type specific effects revealed that a subset of neurons (13 out of 578 cells) responded to tES in a manner opposite to the overall average response of the population (Fig. 3F). While 3 s periods of constant tES induced acute intensity dependent changes in spiking activity during stimulation (Fig. 3E), this tES failed to induce long-lasting effects when comparing spiking activity 30 min before and after tES (n = 575 single units from 4 freely moving rats, Pre: 0.96 ± 0.048 vs. Post: 1.089 ± 0.06 Hz, mean ± SEM, p = 0.38, Wilcoxon rank sum test).

The usual assumption is that pyramidal neurons are preferentially affected by tES due to their morphology [6]. However, tES also affected interneurons, mostly with the same polarity as pyramidal neurons. We hypothesized that this is a consequence of the pyramidal cell activation. To test this, we used transgenic mice where we can selectively stimulate excitatory cells in the CA1 region. We delivered brief pulses of blue light (405 nm, 100 ms, n = 100 trials) in a head-fixed, awake transgenic mouse expressing channelrhodopsin-2 (ChR2) exclusively in CamKII expressing excitatory cells (Suppl. Fig. 9) [35]. As result of this optogenetic stimulation, we observed prominent firing of action potentials both in putative pyramidal cells and in putative interneurons, likely as a result of monosynaptic excitatory drive from the stimulated pyramidal

neurons (Suppl. Fig. 9D, ΔFR = 95.46 and 95.24 % for putative pyramidal cells and interneurons, respectively, median, p = 0.85, n = 65 putative pyramidal cells and n = 11 putative interneurons, Wilcoxon rank sum test).

4. Discussion

First, we calibrated the recording equipment with an in vitro phantom. We also built a computational current-flow model for the rat based on high resolution MRI. This model was calibrated by measuring voltage changes in the motor cortex and hippocampus in anesthetized and freely moving rats during sinusoidal tES. We found that 100 μA currents induced 1.5–3 V/m in motor regions and 1.0–2.0 V/m in the hippocampus. Taking advantage of the 5120 contacts available on Neuropixels2.0 probes, we measured the electric fields using 1536 channels in the hippocampus. As expected from the model, electric fields decrease with distance from the stimulation electrodes. Using large-scale electrophysiology in freely moving rats, we found that neuronal firing was modulated by tES with a monotonic dose-response by about 11 % per V/m. This is above the effect sizes reported in previous in-vitro literature [28] or in-vivo literature [19,56]. The importance of field orientation has been demonstrated repeatedly, starting with Chan and Nicholson (1986) [57]. Previous studies in rodents were either performed under anesthesia [19] or did not optimally align electric fields with the main neural axis [19,56]. Therefore, we ascribe the increased efficacy of the present study to the fact that neurons are closer to firing threshold in the awake state [58,59] and a more careful alignment of electric field orientation to the main neural axis.

Our results here were obtained in the hippocampus but we believe that results should apply similarly to pyramidal cells in the cortex. Like in the hippocampus, cortical pyramidal cells are oriented orthogonally to the surface. Field orientation relative to the cortical surface is therefore the main determining factor of somatic membrane polarization which affects firing rate [60]. In our preparation we found field intensity in cortex and hippocampus to be comparable despite the difference in depth, which the model explains as the result of lower conductivity of hippocampal tissue. Effects of stimulation on the hippocampus are of interest in their own right, given its major role in a variety of neurological and psychiatric disorders.

Local electric field intensity and orientation at the targeted neurons is a key factor affecting the efficacy of neuromodulation [4,61]. Translation of preclinical findings is difficult because in vivo animal experiments have not measured field intensities and estimates suggest that they are ten-fold compared to humans [28]. To bridge the gap between human and animal work, and to increase rigor, it is important to know the actual magnitude and direction of field intensity in the target brain region. We recommend measuring the electric field in situ using sinusoidal waveforms at three different intensities. In order to calibrate the recording hardware [47], we also recommend testing the stimulation and measurement systems (recording electrodes and amplifiers) in a phantom. We measured field intensity intracranially in the motor cortex and hippocampus and built a computational model to match our electrode montages. Using state-of-the-art computer models, we can now estimate the magnitude and spatial distribution of electric fields. Our high-resolution model predicted rebounds in the electric fields (Figs. 1F and 2H). The non-monotonic decrease in electric fields is due to heterogeneous electrical conductivities of the head tissues [62]. This heterogeneity has a significant effect on the electric field distribution during tES [50]. Both the electric field and the current density are boosted in low-conductivity tissues resulting in increased magnitude of the electric fields in the low-conductivity tissue. The maximum value of the electric field occurs at the tissue boundaries [63,64]. These effects are determined by the conductivity of the different tissues and by the shape of their boundaries.

Currently available stimulation electrodes (saline filled cup or epicranial screw electrodes) cannot be combined with large-scale electrophysiology because of physical constraints [65]. To overcome this limitation, we developed a biocompatible permanent gel/electrode enclosure affixed to the skull and combined it with high-channel count electrophysiology and behavior in freely moving rats. This conductive gel loaded chamber provided stable current delivery to the brain and prevented chemical change at the electrode-tissue interface [66]. In many cases this is trivial to manage but with increasing invasive electrodes, higher dose, and irregular placement of electrode/electrolyte, an extreme chemical change could in theory disintegrate the skull and damage the brain.

While it is clear that the efficacy of tES depends on stimulation intensity, duration, polarity, and electrode montage (size, location, and number of electrodes) [67], there is no reliable evidence that higher stimulation intensity is always more effective [68]. The generation of action potentials in vivo depends on the overall synaptic drive, and subthreshold tES-induced electric fields act as a bias to action potential generation. This implies that there is no strict lower threshold for field intensity to modulate the likelihood of action potential generation. However, low intensity tES will succeed only if the neuron membrane is depolarized enough to affect firing (close to its spiking threshold). Our in-vivo measurements in rats showed that low intensity tES (<1 V/m) can have a significant effect on average firing rate. Previous studies have shown that affecting even a small number of neurons has significant behavioral effects. Previous studies have shown that affecting even a small number of neurons has significant behavioral effects [69–71]. While this is true, it is also well established that certain disorders might require the activation of hundreds of thousands of neurons (deep brain stimulation for Parkinson's disease) [72] or more than 10 V/m intracranial fields (tES for absence seizures) [73,74].

The present results may also speak to the long standing debate on the effects of endogenous electric fields on neuronal firing [75]. Electric fields generated during theta rhythms in the hippocampus of rats [75] can be in the range of 1–2 V/m and up to 2 V/m during slow waves in the visual cortex of ferrets [5]. New evidence that such weak fields can have an effect on neuronal function comes from in vitro experiments [5–8] as well as computational modeling [76–78]. These studies mostly demonstrated a modulation of the timing of rhythmic neural activity, and relied on highly coherent rhythms that are not commonly observed in vivo. The present work extends this earlier work by demonstrating effects on firing rate for fields as low as 0.5 V/m at times scales of 3 s in vivo.

A caveat of our study is that we only analyzed acute effects on firing rate, using only short intervals of constant current stimulation (3–4 s). We did not aim to document lasting effects beyond the period of stimulation, although that is the primary goal of most clinical interventions with tES. A prevalent theory for long term effects of direct current tES (tDCS) is that it affects synaptic efficacy [79]. There is ample in-vitro evidence that DCS can boost synaptic plasticity [12,55,80–84]. These effects all involve an acute boost of neuronal firing in pyramidal neurons, not unlike what was observed here. Indeed, modeling studies suggest that the observed synaptic effects are due to only a small subset of active neurons [80]. Effects on synaptic plasticity have been demonstrated in-vitro down to 2.5 V/m [81]. There is no reason why the effects observed here in vivo on firing rate at 0.5 V/m would not similarly affect synaptic plasticity.

We recorded from the intermediate hippocampus because the orientation of pyramidal cells is parallel to the applied fields [16]. This ideal alignment made pyramidal cells more susceptible to electric fields. This effect was the most striking at low tES intensities. Furthermore, neurons are symmetrically located in the left and right intermediate hippocampus providing an experimental setup in which we could test soma-depolarizing and -hyperpolarizing effects simultaneously. Our bilateral hippocampi measurements confirmed that soma-depolarizing and -hyperpolarizing effects are occurring simultaneously in the two hemispheres with opposing signs (depolarizing tES increased, while hyperpolarizing tES decreased the spiking of neurons). On the cortical surface inward current (anodal tES) will depolarize the soma of

pyramidal neurons, while it will hyperpolarize the soma of pyramidal neurons in the hippocampus due to their opposing anatomical orientation [4], and the reverse is true for outward currents (cathodal tES). When stimulation electrodes are placed on the head, it is important to consider both depolarizing and hyperpolarizing effects.

Neurons are embedded in networks that are influenced by tES differently. The effect of electrical stimulation is non-specific affecting any neuronal soma, and depending primarily on cell morphology relative to local field orientation [61]. The symmetric morphology of inter-neuron suggests that their soma is not meaningfully polarized by electric fields. That they responded here similarly to pyramidal neurons is likely the result of monosynaptic drive from excitatory neurons, as we demonstrated with targeted optogenetic stimulation of pyramidal neurons. However, the spike rate increase in interneurons did not always correspond to the spike rate of monosynaptically connected pyramidal cells in the hippocampus. Indeed, pyramidal neurons on opposite hemispheres were positively affected, as expected given their cytoarchitecture. Therefore, the connectivity of individual inter-neurons may be the primary driver of how they respond to tES. A small subset of pyramidal neurons also responded opposite to other pyramidal neurons in their immediate neighborhood. As CA2 is curved it is possible that these pyramidal neurons were not aligned with the field orientation and thus their soma were minimally polarized, so that activated interneurons inhibited their firing. These findings suggest that effects on individual neurons are governed by the orientation and shape of the neuron relative to the electric field, as well as their connectivity to the network of neurons.

In conclusion, we have shown that neuronal firing rates are acutely affected in vivo at clinically relevant field magnitudes providing a viable mechanistic explanation for the effects observed with tES in human experimentation. Future work will need to establish whether these acute effects translate into long term effects, for instance, by modulating synaptic plasticity.

Data availability

The data sets generated and analyzed during the current study are available upon reasonable request from the corresponding authors for further analyses.

CRediT authorship contribution statement

Forouzan Farahani: Formal analysis, Data curation. **Niranjan Khadka:** Formal analysis. **Lucas C. Parra:** Writing – original draft, Conceptualization. **Marom Bikson:** Writing – original draft, Supervision. **Mihály Vöröslakos:** Writing – original draft, Formal analysis, Data curation, Conceptualization.

Declaration of competing interest

LP is listed as inventor in patents owned by CCNY, and has shares in Soterix Medical Inc. The City University of New York (CUNY) has IP on neuro-stimulation systems and methods with authors NK and MB as inventors. NK is an employee of Synchron Inc and consults for Ceragem Medical. MB has equity in Soterix Medical. MB consults, received grants, assigned inventions, and/or served on the S A B of SafeToddles, Boston Scientific, GlaxoSmithKline, Biovisics, Mecta, Lumenis, Halo Neuroscience, Google-X, i-Lumen, Humm, Allergan (Abbvie), Apple, Ybrain, Ceragem Medical, Remz.

Acknowledgements

We thank György Buzsáki for useful comments on the manuscript. This work was supported by NIH through grant R01 NS130484.

Appendix A. Supplementary data

Supplementary data to this article can be found online at https://doi.org/10.1016/j.brs.2024.04.007.

References

[1] Bindman LJ, Lippold OCJ, Redfearn JWT. The action of brief polarizing currents on the cerebral cortex of the rat (1) during current flow and (2) in the production of long-lasting after-effects. J Physiol 1964;172:369–82. https://doi.org/10.1113/jphysiol.1964.sp007425.
[2] Creutzfeldt OD, Fromm GH, Kapp H. Influence of transcortical d-c currents on cortical neuronal activity. Exp Neurol 1962;5:436–52. https://doi.org/10.1016/0014-4886(62)90056-0.
[3] Purpura DP, McMurtry JG. Intracellular activities and evoked potential changes during of motor cortex. Neurophysiology 1965;28:166–85. https://doi.org/10.1152/jn.1965.28.1.166.
[4] Bikson M, Inoue M, Akiyama H, Deans JK, Fox JE, Miyakawa H, et al. Effects of uniform extracellular DC electric fields on excitability in rat hippocampal slices in vitro. J Physiol 2004;557:175–90. https://doi.org/10.1113/jphysiol.2003.055772.
[5] Fröhlich F, McCormick DA. Endogenous electric fields may guide neocortical network activity. Neuron 2010;67:129–43. https://doi.org/10.1016/j.neuron.2010.06.005.
[6] Radman T, Su Y, An JH, Parra LC, Bikson M. Spike timing amplifies the effect of electric fields on neurons: implications for endogenous field effects. J Neurosci 2007;27:3030–6. https://doi.org/10.1523/JNEUROSCI.0095-07.2007.
[7] Reato D, Rahman A, Bikson M, Parra LC. Low-intensity electrical stimulation affects network dynamics by modulating population rate and spike timing. J Neurosci 2010;30:15067–79. https://doi.org/10.1523/JNEUROSCI.2059-10.2010.
[8] Deans JK, Powell AD, Jefferys JGR. Sensitivity of coherent oscillations in rat hippocampus to AC electric fields. J Physiol 2007;583:555–65. https://doi.org/10.1113/jphysiol.2007.137711.
[9] Bikson M, Dmochowski J, Rahman A. The "quasi-uniform" assumption in animal and computational models of non-invasive electrical stimulation. Brain Stimul 2013;6:704–5. https://doi.org/10.1021/nn300902w. Release.
[10] Radman T, Ramos RL, Brumberg JC, Bikson M. Role of cortical cell type and morphology in subthreshold and suprathreshold uniform electric field stimulation in vitro. Brain Stimul 2009;2:215–228.e3. https://doi.org/10.1016/J.BRS.2009.03.007.
[11] Reato D, Bikson M, Parra LC. Lasting modulation of in vitro oscillatory activity with weak direct current stimulation. J Neurophysiol 2015;113:1334–41. https://doi.org/10.1152/jn.00208.2014.
[12] Farahani F, Kronberg G, FallahRad M, Oviedo HV, Parra LC. Effects of direct current stimulation on synaptic plasticity in a single neuron. Brain Stimul 2021;14:588–97. https://doi.org/10.1016/j.brs.2021.03.001.
[13] Ozen S, Sirota A, Belluscio MA, Anastassiou CA, Stark E, Koch C. Transcranial electric stimulation entrains cortical neuronal populations in rats. J Neurosci 2010;30:11476–85. https://doi.org/10.1523/JNEUROSCI.5252-09.2010.
[14] Rohan JG, Carhuatanta KA, McInturf SM, Miklasevich MK, Jankord R. Modulating hippocampal plasticity with in vivo brain stimulation. J Neurosci 2015;35:12824–32. https://doi.org/10.1523/JNEUROSCI.2376-15.2015.
[15] Johnson L, Alekseichuk I, Krieg J, Doyle A, Yu Y, Vitek J, et al. Dose-dependent effects of transcranial alternating current stimulation on spike timing in awake nonhuman primates. Sci Adv 2020;6:1–9. https://doi.org/10.1126/sciadv.aaz2747.
[16] Chan CY, Nicholson C. Modulation by applied electric fields of Purkinje and stellate cell activity in the isolated turtle cerebellum. J Physiol 1986;371:89–114.
[17] Asan AS, Gok S, Sahin M. Electrical fields induced inside the rat brain with skin, skull, and dural placements of the current injection electrode. PLoS One 2019;14:1–15. https://doi.org/10.1371/journal.pone.0203727.
[18] Binder S, Berg K, Gasca F, Lafon B, Parra LC, Born J, et al. Transcranial slow oscillation stimulation during sleep enhances memory consolidation in rats. Brain Stimul 2014;7:508–15. https://doi.org/10.1016/j.brs.2014.03.001.
[19] Vöröslakos M, Takeuchi Y, Brinyiczki K, Zombori T, Oliva A, Fernández-Ruiz A, et al. Direct effects of transcranial electric stimulation on brain circuits in rats and humans. Nat Commun 2018;9:483. https://doi.org/10.1038/s41467-018-02928-3.
[20] Mishima T, Nagai T, Yahagi K, Akther S, Oe Y, Monai H, et al. Transcranial direct current stimulation (tDCS) induces adrenergic receptor-dependent microglial morphological changes in mice. ENeuro 2019;6:1–12. https://doi.org/10.1523/ENEURO.0204-19.2019.
[21] Gellner AK, Reis J, Holtick C, Schubert C, Fritsch B. Direct current stimulation-induced synaptic plasticity in the sensorimotor cortex: structure follows function. Brain Stimul 2020;13:80–8. https://doi.org/10.1016/j.brs.2019.07.026.
[22] Huang WA, Stitt IM, Negahbani E, Passey DJ, Ahn S, Davey M, et al. Transcranial alternating current stimulation entrains alpha oscillations by preferential phase synchronization of fast-spiking cortical neurons to stimulation waveform. Nat Commun 2021. https://doi.org/10.1038/s41467-021-23021-2.
[23] Fritsch B, Gellner AK, Reis J. Transcranial electrical brain stimulation in alert rodents. J Vis Exp 2017;2017:1–10. https://doi.org/10.3791/56242.
[24] Podda MV, Cocco S, Mastrodonato A, Fusco S, Leone L, Barbati SA, et al. Anodal transcranial direct current stimulation boosts synaptic plasticity and memory in mice via epigenetic regulation of Bdnf expression. Sci Rep 2016;6:22180. https://doi.org/10.1038/srep22180.

[25] Sharma M, Farahani F, Bikson M, Parra LC. Animal studies on the mechanisms of low-intensity transcranial electric stimulation. In: Brunoni AR, Nitsche MA, Loo CK, editors. Transcranial direct curr. Stimul. Neuropsychiatr. Disord. Second. Springer; 2021.

[26] Opitz A, Falchier A, Yan C, Yeagle E, Linn G. Spatiotemporal structure of intracranial electric fields induced by transcranial electric stimulation in human and nonhuman primates. Sci Rep 2016;6:1–11. https://doi.org/10.1101/053892.

[27] Huang Y, Liu AA, Lafon B, Friedman D, Dayan M, Wang X, et al. Measurements and models of electric fields in the in vivo human brain during transcranial electric stimulation. Elife 2017;6:1–26. https://doi.org/10.7554/eLife.18834.

[28] Liu A, Vöröslakos M, Kronberg G, Henin S, Krause MR, Huang Y, et al. Immediate neurophysiological effects of transcranial electrical stimulation. Nat Commun 2018;9. https://doi.org/10.1038/s41467-018-07233-7.

[29] Steinmetz NA, Aydin C, Lebedeva A, Okun M, Pachitariu M, Bauza M, et al. Neuropixels 2.0: a miniaturized high-density probe for stable, long-term brain recordings. Science (80-) 2021;372. https://doi.org/10.1126/science.abf4588.

[30] Pachitariu M, Steinmetz N, Kadir S, Carandini M, Harris KD. Kilosort: realtime spike-sorting for extracellular electrophysiology with hundreds of channels. bioRxiv 2016:061481. https://doi.org/10.1101/061481.

[31] Henze DA, Borhegyi Z, Csicsvari J, Mamiya A, Harris KD, Buzsáki G. Intracellular features predicted by extracellular recordings in the Hippocampus in vivo. J Neurophysiol 2000;84:390–400. https://doi.org/10.1152/jn.2000.84.1.390.

[32] Stark E, Eichler R, Roux L, Fujisawa S, Rotstein HG, Buzsáki G. Inhibition-Induced theta resonance in cortical circuits. Neuron 2013;80:1263–76. https://doi.org/10.1016/j.neuron.2013.09.033.

[33] English DF, McKenzie S, Evans T, Kim K, Yoon E, Buzsáki G. Pyramidal cell-interneuron circuit architecture and dynamics in hippocampal networks. Neuron 2017;96:505–520.e7. https://doi.org/10.1016/j.neuron.2017.09.033.

[34] Huszár R, Zhang Y, Blockus H, Buzsáki G. Preconfigured dynamics in the hippocampus are guided by embryonic birthdate and rate of neurogenesis. Nat Neurosci 2022;25:1201–12. https://doi.org/10.1038/s41593-022-01138-x.

[35] Vöröslakos M, Kim K, Slager N, Ko E, Oh S, Parizi SS, et al. HectoSTAR μLED optoelectrodes for large-scale, high-precision in vivo opto-electrophysiology. Adv Sci 2022;2105414:2105414. https://doi.org/10.1002/advs.202105414.

[36] Schneiders NJ. Solutions of two paramagnetic ions for use in nuclear magnetic resonance phantoms. Med Phys 1988;15:12–6.

[37] Seymour JP, Wu F, Wise KD, Yoon E. State-of-the-art mems and microsystem tools for brain research. Microsystems Nanoeng 2017;3:1–16. https://doi.org/10.1038/micronano.2016.66.

[38] Christoffersson JO, Olsson LE, Sjöberg S. Nickel-doped agarose gel phantoms in MR imaging. Acta Radiol 1991;32:426–31. https://doi.org/10.1177/028418519103200519.

[39] Vöröslakos M, Petersen PC, Vöröslakos B, Buzsáki G. Metal microdrive and head cap system for silicon probe recovery in freely moving rodent. Elife 2021;10:1–21. https://doi.org/10.7554/eLife.65859.

[40] Jun JJ, Steinmetz NA, Siegle JH, Denman DJ, Bauza M, Barbarits B, et al. Fully integrated silicon probes for high-density recording of neural activity. Nature 2017;551:232–6. https://doi.org/10.1038/nature24636.

[41] Siegle JH, López AC, Patel YA, Abramov K, Ohayon S, Voigts J. Open Ephys: an open-source, plugin-based platform for multichannel electrophysiology. J Neural Eng 2017;14. https://doi.org/10.1088/1741-2552/aa5eea.

[42] Petersen PC, Siegle JH, Steinmetz NA, Mahallati S, Buzsáki G. CellExplorer: a framework for visualizing and characterizing single neurons. Neuron 2021;109:3594–3608.e2. https://doi.org/10.1016/j.neuron.2021.09.002.

[43] English DF, Peyrache A, Stark E, Roux L, Vallentin D, Long MA, et al. Excitation and inhibition compete to control spiking during hippocampal ripples: intracellular study in behaving mice. J Neurosci 2014;34:16509–17. https://doi.org/10.1523/JNEUROSCI.2600-14.2014.

[44] Sirota A, Montgomery S, Fujisawa S, Isomura Y, Zugaro M, Buzsáki G. Entrainment of neocortical neurons and gamma oscillations by the hippocampal theta rhythm. Neuron 2008;60:683–97. https://doi.org/10.1016/J.NEURON.2008.09.014.

[45] Barthó P, Hirase H, Monconduit L, Zugaro M, Harris KD, Buzsáki G. Characterization of neocortical principal cells and interneurons by network interactions and extracellular features. J Neurophysiol 2004;92:600–8. https://doi.org/10.1152/jn.01170.2003.

[46] Hadar R, Winter R, Edemann-Callesen H, Wieske F, Habelt B, Khadka N, et al. Prevention of schizophrenia deficits via non-invasive adolescent frontal cortex stimulation in rats. Mol Psychiatr 2020;25:896–905. https://doi.org/10.1038/s41380-019-0356-x.

[47] FallahRad M, Zannou AL, Khadka N, Prescott SA, Ratté S, Zhang T, et al. Electrophysiology equipment for reliable study of kHz electrical stimulation. J Physiol 2019;597:2131–7. https://doi.org/10.1113/JP277654.

[48] Wang B, Peterchev AV, Gaugain G, Ilmoniemi RJ, Grill WM, Bikson M, et al. Quasistatic approximation in neuromodulation. Arxiv 2024.

[49] Datta A, Bansal V, Diaz J, Patel J, Reato D, Bikson M. Gyri –precise head model of transcranial DC stimulation: improved spatial focality using a ring electrode versus conventional rectangular pad. Brain Stimul 2009;2:201–7. https://doi.org/10.1016/j.brs.2009.03.005.Gyri.

[50] Miranda PC, Hallett M, Basser PJ. The electric field induced in the brain by magnetic stimulation: a 3-D finite-element analysis of the effect of tissue heterogeneity and anisotropy. IEEE Trans Biomed Eng 2003;50:1074–85. https://doi.org/10.1109/TBME.2003.816079.

[51] Mizuseki K, Diba K, Pastalkova E, Buzsáki G. Hippocampal CA1 pyramidal cells form functionally distinct sublayers. Nat Neurosci 2011;14:1174–83. https://doi.org/10.1038/nn.2894.

[52] Buzsáki G, Leung LW, Vanderwolf CH. Cellular bases of hippocampal EEG in the behaving rat. Brain Res 1983;287:139–71. https://doi.org/10.1016/0165-0173(83)90037-1.

[53] Buzsáki G. Hippocampal sharp wave-ripple: a cognitive biomarker for episodic memory and planning. Hippocampus 2015;25:1073–188. https://doi.org/10.1002/hipo.22488.

[54] Csicsvari J, Henze DA, Jamieson B, Harris KD, Sirota A, Barthó P, et al. Massively parallel recording of unit and local field potentials with silicon-based electrodes. J Neurophysiol 2003;90:1314–23. https://doi.org/10.1152/jn.00116.2003.

[55] Rahman A, Lafon B, Parra LC, Bikson M. Direct current stimulation boosts synaptic gain and cooperativity in vitro. J Physiol 2017;595:3535–47. https://doi.org/10.1113/JP273005.

[56] Milighetti S, Sterzi S, Fregni F, Hanlon CA, Hayley P, Murphy MD, et al. Effects of tDCS on spontaneous spike activity in a healthy ambulatory rat model. Brain Stimul 2020;13:1566–76. https://doi.org/10.1016/j.brs.2020.08.016.

[57] Chan CY, Nicholson C. Modulation by applied electric fields of Purkinje and stellate cell activity in the isolated turtle cerebellum. J Physiol 1986;371:89–114. https://doi.org/10.1113/jphysiol.1986.sp015963.

[58] Steriade M, Timofeev I, Grenier F. Natural waking and sleep states: a view from inside neocortical neurons. J Neurophysiol 2001;85:1969–85. https://doi.org/10.1152/jn.2001.85.5.1969.

[59] Destexhe A, Rudolph M, Paré D. The high-conductance state of neocortical neurons in vivo. Nat Rev Neurosci 2003;4:739–51. https://doi.org/10.1038/nrn1198.

[60] Rahman A, Reato D, Arlotti M, Gasca F, Datta A, Parra LC, et al. Cellular effects of acute direct current stimulation: somatic and synaptic terminal effects. J Physiol 2013;591:2563–78. https://doi.org/10.1113/jphysiol.2012.247171.

[61] Radman T, Ramos RL, Brumberg JC, Bikson M. Role of cortical cell type and morphology in subthreshold and suprathreshold uniform electric field stimulation in vitro. Brain Stimul 2009;2:215–28. https://doi.org/10.1016/j.brs.2009.03.007. 228.e1-3.

[62] Gabriel C, Gabriel S, Corthout E. The dielectric properties of biological tissues: I. Literature survey. Phys Med Biol 1996;41:2231–49.

[63] Wagner TA, Zahn M, Grodzinsky AJ, Pascual-Leone A. Three-dimensional head model simulation of transcranial magnetic stimulation. IEEE Trans Biomed Eng 2004;51:1586–98. https://doi.org/10.1109/TBME.2004.827925.

[64] Heller L, van Hulsteyn DB. Brain stimulation using electromagnetic sources: theoretical aspects. Biophys J 1992;63:129–38. https://doi.org/10.1016/S0006-3495(92)81587-4.

[65] Jackson MP, Rahman A, Lafon B, Kronberg G, Ling D, Parra LC, et al. Animal models of transcranial direct current stimulation: methods and mechanisms. Clin Neurophysiol 2016;127:3425–54. https://doi.org/10.1016/j.clinph.2016.08.016.

[66] Merrill DR, Bikson M, Jefferys JGR. Electrical stimulation of excitable tissue: design of efficacious and safe protocols. J Neurosci Methods 2005;141:171–98. https://doi.org/10.1016/j.jneumeth.2004.10.020.

[67] Peterchev AV, Wagner TA, Miranda PC, Nitsche MA, Paulus W, Lisanby SH, et al. Fundamentals of transcranial electric and magnetic stimulation dose: definition, selection, and reporting practices. Brain Stimul 2012;5:435–53. https://doi.org/10.1016/j.brs.2011.10.001.

[68] Esmaeilpour Z, Marangolo P, Hampstead BM, Bestmann S, Galletta E, Knotkova H, et al. Incomplete evidence that increasing current intensity of tDCS boosts outcomes. Brain Stimul 2018;11:310–21. https://doi.org/10.1016/J.BRS.2017.12.002.

[69] Houweling AR, Brecht M. Behavioural report of single neuron stimulation in somatosensory cortex. Nature 2008;451:65–8. https://doi.org/10.1038/nature06447.

[70] Huber D, Petreanu L, Ghitani N, Ranade S, Hromádka T, Mainen Z, et al. Sparse optical microstimulation in barrel cortex drives learned behaviour in freely moving mice. Nature 2008;451:61–4. https://doi.org/10.1038/nature06445.

[71] Ledford H. The power of a single number. Nat News 2007. https://doi.org/10.7312/columbia/9780231175104.001.0001.

[72] Chaturvedi A, Butson CR, Lempka SF, Cooper SE, McIntyre CC. Patient-specific models of deep brain stimulation: influence of field model complexity on neural activation predictions. Brain Stimul 2010;3:65–77. https://doi.org/10.1016/j.brs.2010.01.003.

[73] Kozák G, Berényi A. Sustained efficacy of closed loop electrical stimulation for long-term treatment of absence epilepsy in rats. Sci Rep 2017;7:1–10. https://doi.org/10.1038/s41598-017-06684-0.

[74] Berényi A, Belluscio M, Mao D, Buzsáki G. Closed-loop control of epilepsy by transcranial electrical stimulation. Science 2012;337(80-):735–7. https://doi.org/10.1126/science.1223154.

[75] Jefferys JGR. Nonsynaptic modulation of neuronal activity in the brain : electric currents and extracellular ions. Physiol Rev 1995;75:689–723.

[76] Qiu C, Shivacharan RS, Zhang M, Durand DM. Can neural activity propagate by endogenous electrical field? J Neurosci 2015;35:15800–11. https://doi.org/10.1523/JNEUROSCI.1045-15.2015.

[77] Pinotsis DA, Miller EK. In vivo ephaptic coupling allows memory network formation. Cerebr Cortex 2023;33:9877–95. https://doi.org/10.1093/cercor/bhad251.

[78] Anastassiou CA, Koch C. Ephaptic coupling to endogenous electric field activity: why bother? This review comes from a themed issue on Brain rhythms and dynamic coordination. Curr Opin Neurobiol 2015;31:95–103. https://doi.org/10.1016/j.conb.2014.09.002.

[79] Stagg CJ, Nitsche MA. Physiological basis of transcranial direct current stimulation. Neuroscientist 2011;17:37–53. https://doi.org/10.1177/1073858410386614.

[80] Kronberg G, Rahman A, Sharma M, Bikson M, Parra LC. Direct current stimulation boosts hebbian plasticity in vitro. Brain Stimul 2020;13:287–301. https://doi.org/10.1016/j.brs.2019.10.014.
[81] Sharma M, Farahani F, Bikson M, Parra LC. Weak DCS causes a relatively strong cumulative boost of synaptic plasticity with spaced learning. Brain Stimul 2022;15:57–62. https://doi.org/10.1016/j.brs.2021.10.552.
[82] Kronberg G, Bridi M, Abel T, Bikson M, Parra LC. Direct current stimulation modulates LTP and LTD: activity dependence and dendritic effects. Brain Stimul 2017;10:51–8. https://doi.org/10.1016/j.brs.2016.10.001.
[83] Fritsch B, Reis J, Martinowich K, Schambra HM, Ji Y, Cohen LG, et al. Direct current stimulation promotes BDNF-dependent synaptic plasticity: potential implications for motor learning. Neuron 2010;66:198–204. https://doi.org/10.1016/j.neuron.2010.03.035.
[84] Ranieri F, Podda MV, Riccardi E, Frisullo G, Dileone M, Profice P, et al. Modulation of LTP at rat hippocampal CA3-CA1 synapses by direct current stimulation. J Neurophysiol 2012;107:1868–80. https://doi.org/10.1152/jn.00319.2011.